Tuning the spectral response of ultraviolet organic-inorganic hybrid photodetectors via charge trapping and charge collection narrowing

Journal:	*Physical Chemistry Chemical Physics*
Manuscript ID	CP-ART-01-2018-000361.R1
Article Type:	Paper
Date Submitted by the Author:	13-Mar-2018
Complete List of Authors:	Esopi, Monica; University of Washington, Chemical Engineering Zheng, Erjin; University of Washington, Chemical Engineering Zhang, Xiaoyu; University of Washington, Chemical Engineering Cai, Chen; University of Washington, Chemical Engineering Yu, Qiuming; University of Washington, Chemical Engineering

Journal Name

ARTICLE

Tuning the spectral response of ultraviolet organic-inorganic hybrid photodetectors via charge trapping and charge collection narrowing

Received 00th January 20xx,
Accepted 00th January 20xx

DOI: 10.1039/x0xx00000x

www.rsc.org/

Monica R. Esopi, Erjin Zheng, Xiaoyu Zhang, Chen Cai, and Qiuming Yu*

Organic-inorganic hybrid ultraviolet photodetectors with tunable spectral response are desirable for many different applications. In this work, we blended poly[bis(4-phenyl)(2,4,6-trimethylphenyl)amine] (PTAA) with ZnO nanoparticles in weight ratios of 1:1 and 2:1 to create charge traps within the active layers for devices with the conventional structure ITO/PEDOT:PSS/PTAA:ZnO/BCP/Al. Thin (150-200 nm) and thick (1400-1900 nm) active layers were employed to utilize charge collection narrowing (CCN). Both thickness and composition of the active layer impacted the spectral tunability of the photoresponse. A single narrow response peak centered at 420 nm (the PTAA absorption edge) with a full width at half maximum of 12 nm was achieved from the device with a 1900 nm active layer and PTAA:ZnO weight ratio of 1:1. Decreasing the active layer thickness to 150 nm resulted in a broad spectral response between 320-420 nm with an external quantum efficiency (EQE) value of 295% under 350 nm illumination and a -1 V bias, exhibiting photomultiplication via charge trapping and injection even at small reverse biases. Increasing the weight ratio of PTAA:ZnO to 2:1 lowered both the dark current and photocurrent, eliminated photomultiplication in the thin device, and diminished the efficacy of CCN to narrow the spectral photoresponse in the thick device. Transfer matrix method (TMM) and 3-dimensional finite-difference time-domain (3D-FDTD) simulations were performed to understand the impact of thickness and composition of the active layer on the spectral response of UV photodetectors in terms of exciton generation rate and electric field distribution within the devices.

Introduction

There are many advantages to using organic materials and organic-inorganic hybrids in optoelectronic devices, including low material cost, easy processing and fabrication, and flexibility[1]. Another commonly touted benefit is the tunability of the optical characteristics of organic materials. For ultraviolet (UV) photodetectors, applications like environmental monitoring and laboratory instrumentation require a broadband UV response, while applications like filter-free imaging and colorimetry require wavelength-specific narrowband response[1]. It is therefore desirable to produce devices based on organic materials that have a strong photoresponse, and even more desirable to produce devices with responses that are tunable and UV-selective.

Organic photodetectors with broad spectral response from UV to near infrared (NIR) were first demonstrated by the Heeger group, using a narrow-bandgap conjugated polymer, poly(5,7-bis(4-decanyl-2-thienyl)-thieno(3,4-b)diathiazole-thiophene-2,5) (PDDTT), blended with [6,6]phenyl-C_{61}-butyric acid methyl ester ($PC_{60}BM$) in a 1:1 weight ratio as the active layer[2]. The device had a structure of indium tin oxide (ITO)/poly(3,4-ethylenedioxythiophene) polystyrene sulfonate (PEDOT:PSS) /PDDTT:$PC_{60}BM$/Al and produced photoresponse ranging from 300-1450 nm with specific detectivity (D*) values exceeding 10^{12} Jones throughout the entire range[2]. Since then, organic-inorganic hybrid systems have also been used to fabricate broadband photodetectors, including many that incorporate quantum dots (QDs) into polymer active layers[3]. The integration of CdSe QDs into a layer of poly(2-methoxy,5-(2'-ethyl-hexyloxy)-p-phenylenevinylene) (MEH-PPV) broadened the device photoresponse from a relatively narrow peak centered around 550 nm to a broader peak from 420 to 650 nm due to the optical absorption of the QDs[4]. PbS QDs were incorporated into a P3HT:PCBM blend active layer, resulting in devices with NIR response that could be tuned to extend from 1000 nm to 1200-1700 nm depending on the size of the PbS QDs[5].

Various mechanisms have been employed to tune photodetector response to a narrow wavelength range. Typically, a full width at half maximum (FWHM) around or below 100 nm is desired for narrowband devices. One method of achieving this narrow response is focusing on the absorption of the active layer materials. A new squarylium

Department of Chemical Engineering, University of Washington, Seattle, WA 98195, USA

Electronic Supplementary Information (ESI) available: nanoparticle distribution; optical constants for blend thin films; device performance under strong biases; simulated electric field distributions; current density-voltage characteristics for different compositions; noise current plots. See DOI: 10.1039/x0xx00000x

material was recently reported and utilized in thin-film devices producing external quantum efficiency (EQE) spectra with a 110 nm FWHM centered around 600 nm, peaking at 66% under a -2.5 V bias[6]. ZnO nanoparticles have also been incorporated into poly(9,9-di-noctylfluorenyl-2,7-diyl) (PFO) and [9,9'-dioctyl-fluorene-2,7-diyl]-copoly[diphenyl-p-tolyl-amine-4,4'-diyl] (BFE) active layers with a device structure of ITO/PEDOT:PSS/active layer/BCP/Al[7]. These devices were illuminated from both the ITO and Al sides and produced broad UV photoresponse, spanning wavelength ranges of approximately 275-425 nm when illuminated from the ITO side, and 250-425 nm when illuminated from the Al side[7]. In other systems, active layer thickness and composition were controlled to achieve photoresponse narrowing and enhancement. One photoresponse mechanism relied on CdTe quantum dots acting as electron traps within a blended active layer of P3HT and PCBM[8, 9]. In devices with thinner active layers around 200-250 nm, the addition of CdTe quantum dots increased the EQE values from 40-70% to around 1000% under illumination between 350-650 nm and a -1 V bias[9]. In devices having active layer thicknesses around 3 μm, the active layer morphology was such that the CdTe quantum dots were concentrated towards the top of the thick active layer[8]. In this case, only light at the red edge of the P3HT:PCBM absorption peak with a long penetration depth could generate a significant response, resulting in EQE spectra with narrowed response between about 650-750 nm[8].

The active layer thickness itself can also be used to achieve the desired photoresponse tuning and narrowing. Increasing the thickness of the active layer can cause a narrowing in the photoresponse of the device caused by a mechanism called charge collection narrowing (CCN)[10]. For very thick active layers, light within the absorption peak of the active layer is absorbed quickly and does not penetrate far into the active layer, and thus it cannot generate a photoresponse. Light on the edge of the absorption peak, however, penetrates the entire active layer. This light then reflects back into the active layer from the top metal electrode, establishing an interference pattern throughout the active layer. Because of this, it can be absorbed and generate excitons all throughout the active layer, resulting in photoresponse only at this long wavelength at the edge of the absorption peak. The CNN mechanism was first demonstrated in devices with thick active layers (1.5, 2 and 3 μm) composed of (poly[N-900-heptadecanyl-2,7-carbazole-alt-5,5-(40,70-di-2-thienyl-20,10,30-benzothiadiazole) (PCDTBT) and poly[2,5-(2-octyldodecyl)-3,6-diketopyrrolopyrrole-alt-5,5-(2,5-di(thien-2-yl)thieno[3,2-b]thiophene)] (DPP-DTT) blended with $PC_{71}BM$ in weight ratios of 1:4 and 1:3, respectively[10]. These devices had photoresponses that specifically narrowed to the edge of the absorption peak for each polymer, producing red (~650 nm) and NIR (~950 nm) photodetectors with FWHM values around 70 and 90 nm, respectively[10].

In this work, we investigated the spectral response tunability of organic-inorganic hybrid UV photodetectors composed of a wide-bandgap polymer poly[bis(4-phenyl)(2,4,6-trimethylphenyl)amine] (PTAA) blended with ZnO nanoparticles as the active layer in a device with a structure of ITO/PEDOT:PSS/PTAA:ZnO/BCP/Al. PTAA and ZnO were blended in 1:1 and 2:1 weight ratios, and both thin (150-200 nm) and thick (1400-1900 nm) active layers were used. By changing the active layer thickness, we can utilize CCN for UV photodetectors and narrow the photoresponse to the absorption edge of the active layer. The composition of the active layer, controlling the microstructure and thus charge transport properties, determined the efficacy of CCN in these devices. In addition to enabling and controlling photoresponse tunability, active layer thickness and composition also impacted the dark current, responsivity (R), specific detectivity (D*), response speed, and stability of devices. Through transfer matrix method (TMM) and 3-dimensional finite-difference time-domain (3D-FDTD) simulations, we predicted that controlling the active layer thickness and composition would enable tuning between a broad photomultiplicative photoresponse and a selective narrowband photoresponse, which we achieved experimentally. This tunability, achieved by changing the simple conditions of active layer composition and thickness, could enable simple and cost-effective production of a variety of UV photodetectors.

Experimental

Materials

ITO-coated glass (≤ 10 Ω sq^{-1}) was purchased from Colorado Concept Coatings LLC (Loveland, CO). Poly(3,4-ethylenedioxythiophene)-poly(styrenesulfonate) (PEDOT:PSS) solution (Clevios P VP AI 4083) was purchased from Heraeus (Hanau, Germany). Anhydrous 1,2-dichlorobenzene (1,2-DCB) of 99.9% purity and bathocuproine (BCP) were purchased from Sigma-Aldrich (St. Louis, MO). Poly[bis(4-phenyl)(2,4,6-trimethylphenyl)amine] (PTAA) was purchased from Solaris Chem. Inc. (Quebec, Canada). Aluminum pellets of 99.999% purity were purchased from R.D. Mathis (Long Beach, CA). ZnO nanoparticles were synthesized according to the procedure previously reported[11]. Briefly, 2.36 g of zinc acetate dihydrate (≥ 99.0%, Sigma-Aldrich) was dissolved in 100 mL of methanol (≥ 99.9%, Fisher Scientific (Hampton, NH)) at 60°C, and 1.256 g KOH (≥ 85.0%, Fischer Scientific) was dissolved in 52 mL of methanol. The two solutions were combined and stirred at 60°C for 1.5 h, at which point the solution became turbid and was stirred for an additional hour. The ZnO nanoparticles were then collected by centrifuge, washed three times in methanol, dissolved in 1,2-DCB at 200 mg mL^{-1}, and stored in a refrigerator until use. The hydrodynamic diameter of the nanoparticles was determined using dynamic light scattering (DLS) with Malvern Zetasizer Nano.

Precursor Solution Preparation

All solution preparation took place in a nitrogen-filled glovebox. The polymer PTAA and ZnO nanoparticles were each dissolved separately in 1,2-DCB with concentrations of 40 mg mL^{-1} and 200 mg mL^{-1}, respectively. The ZnO nanoparticle solution was prepared at room temperature, and the PTAA solution was stirred for at least 12 h at 70°C. Before combining

the two solutions, the PTAA solution was cooled to room temperature. The solutions were combined so that the resulting solution would have either a 1:1 or 2:1 weight ratio with total concentrations of 66.7 mg mL^{-1} and 55.6 mg mL^{-1}, respectively. The combined solution was stirred at room temperature for 5 min before use.

Film Fabrication and Characterization

Plain glass slides were cut and cleaned by ultrasonication for 15 min each in soapy deionized (DI) water, DI water, acetone, and isopropanol, in sequence, and then by oxygen plasma cleaning at 100 W for 30 s. The PTAA:ZnO blend precursor solutions were filtered through a 0.45 μm PTFE syringe filter and deposited via spin coating. For thin films, the precursor solution with a weight ratio of 1:1 or 2:1 was spun at 1000 RPM or 800 RPM, respectively, for 30 s. For thick films, the precursor solutions for both weight ratios of 1:1 and 2:1 were spun at 400 RPM for 30 s. All films were annealed at 100°C for 10 min. All film fabrication steps, after the preparation of the substrates, were done in a nitrogen-filled glovebox. Film analysis was performed in ambient conditions. UV/Vis spectra were collected using a Perkin Elmer Lambda 900 UV/Vis spectrophotometer. Film thicknesses were measured using a KLA Tencor Alpha-Step 500 Profiler. Optical constants of refractive index, n, and extinction coefficient, k, for films were obtained via ellipsometry using a Woollam M-2000 Spectroscopic Ellipsometer. The distribution of ZnO nanoparticles in the thick active layer films was determined with the elemental analysis using energy dispersive X-ray spectroscopy (EDS) on an FEI Sirion scanning electron microscope (SEM).

Device Fabrication

Indium tin oxide (ITO) coated glass substrates were prepared by the same methods of ultrasonication and plasma treatment as the glass substrates used for film fabrication. PEDOT:PSS solution was filtered through a 0.45 μm PTFE syringe filter and spin-coated on the cleaned ITO-coated glass substrates at 5000 RPM for 40 s, then baked at 120°C for 10 min in air. The chips were then transferred into a nitrogen-filled glovebox. The PTAA:ZnO active layers were deposited via spin coating, under the same conditions as the previously described films. A 10 nm layer of BCP was deposited via thermal evaporation, without the use of any mask. Finally, 100 nm aluminum electrodes were deposited via thermal evaporation with rectangular masks to define a 0.1 cm^2 device active area.

Device Characterization

All device characterizations were performed in ambient conditions. Current density versus voltage curves, dark current versus time, and EQE spectra were obtained using a Keithley 2635B sourcemeter. Light was provided with a 150 W Xenon arc lamp and an Oriel Cornerstone 130 Monochromator. Optical intensity was measured using a Newport 1918-R Power Meter and Newport UV-Si Photodiode. The on-off response of the devices was obtained using a Tektronix TBS 1052B Digital Oscilloscope and a chopper controlled by a Stanford Research Systems, Inc Model SR540 Chopper Controller. Bias was applied using the Keithley 2635B sourcemeter. The rise (fall) times are defined as the amount of time it takes for the device to transition from 10% to 90% (90% to 10%) of the photoresponse cycle. Matlab was used to perform Fast Fourier Transform (FFT) on dark current versus time data to obtain noise currents.

Optical and Electromagnetic Simulations

Transfer matrix method[12, 13] (TMM) and 3-dimensional finite-difference time-domain (3D-FDTD, Lumerical FDTD Solutions) simulations were performed to obtain the exciton generation rate and electric field distribution, respectively, within the devices. The simulated devices have a similar structure as those experimentally fabricated, with the same active layer compositions and thicknesses. Specifically, they are glass (100 nm)/ITO (100 nm)/PEDOT:PSS (40 nm)/PTAA:ZnO (weight ratio and thickness varied)/Al (100 nm). The thin BCP layer was not included. The wavelength dependent refractive index, n, and extinction coefficient, k, of active layers were measured experimentally and used in both simulations. The exciton generation rate was calculated for incident light at 375 and 425 nm. Electric field distributions were collected with a frequency-domain field monitor positioned at a cross section through the middle of simulated devices. A plane wave light source (200-700 nm) was positioned 600 nm below the glass layer of the device. Symmetric and anti-symmetric boundary conditions were used in the x and y directions, respectively, and perfectly matched layer boundary conditions were used in the z direction.

Results and Discussion

The UV photodetectors have the structure of ITO/PEDOT:PSS/PTAA:ZnO/BCP/Al, shown in Fig. 1a. The ZnO nanoparticles had an approximate hydrodynamic diameter of 10 nm, and their distribution in the thick active layers is given in Fig. S1. The energy diagram for each layer in the device is shown in Fig. 1b. The work function of PEDOT:PSS was provided by the vendor, as were the highest occupied molecular orbital (HOMO) and lowest unoccupied molecular orbital (LUMO) levels for BCP and PTAA. Values were taken from the literature for the work function of ITO[14, 15] and Al[16], and for HOMO and LUMO levels of ZnO[17, 18]. ZnO is typically an n-type wide-bandgap material with a band gap of 3.3 eV and electron mobility on the order of 1-10 $cm^2 V^{-1} s^{-1}$ [19]. PTAA has been widely used as a hole transport material in perovskite photovoltaic devices[20] because of its hole mobility, which is around $5x10^{-3}$ $cm^2 V^{-1} s^{-1}$ [21]. PTAA is also a wide-bandgap material with a band gap around 3.0 eV. As shown in Fig. 1c, the ZnO nanoparticle thin film has strong UV absorption, with a sharp cutoff around 360 nm. The PTAA thin film absorbs light from about 300-420 nm with the absorption peak around 375 nm and a soft cutoff around 420 nm. The absorption spectra of the blended PTAA and ZnO resemble the absorption spectrum of a PTAA thin film with a peak around 375 nm. The addition of

ZnO nanoparticles extends the absorption deeper into the UV range and makes the absorption edge sharper around 420 nm.

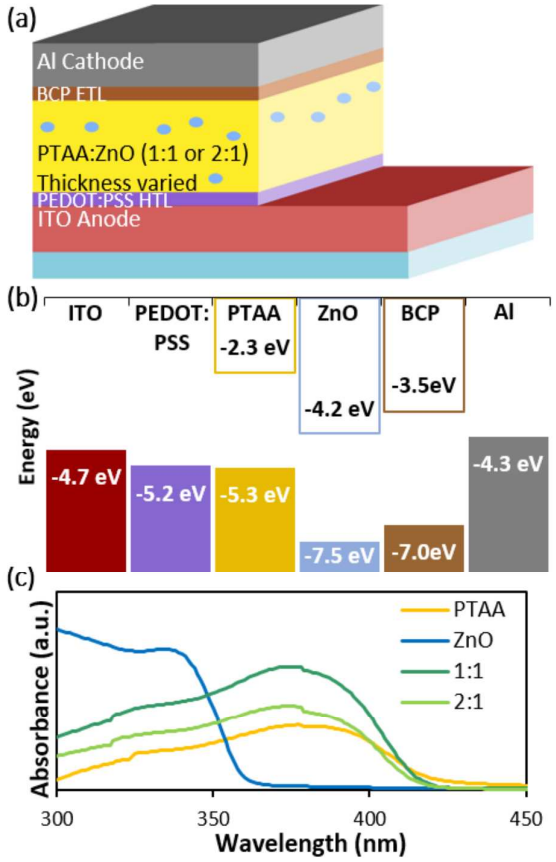

Fig. 1 (a) Schematic of the device structure. (b) Energy levels for each layer in the device. (c) The UV/Vis absorption spectra of ZnO thin nanoparticle film (270 nm), PTAA thin film (30 nm), and PTAA:ZnO thin films with weight ratios of 1:1 (150 nm) and 2:1 (200 nm). The absorbance values were normalized by the absorption at 600 nm for each film.

TMM and 3D-FDTD simulations were used to fully investigate and understand the spectral response as a function of active layer thickness and composition. Two dramatically different active layer thicknesses were used for each weight ratio in these simulations, guided by the thicknesses of fabricated films for each composition: 150 (1:1 weight ratio), 200 (2:1 weight ratio), 1900 (1:1 weight ratio), and 1400 nm (2:1 weight ratio) were used as the active layer thicknesses for Devices 150-1:1, 200-2:1, 1900-1:1, and 1400-2:1, respectively. For both TMM and 3D-FDTD simulations, the wavelength dependent refractive index and extinction coefficient of the PTAA:ZnO (1:1 and 2:1) films were obtained experimentally through ellipsometry, and are shown in Fig. S2. The exciton generation rates within the active layers induced by the light at two different wavelengths, 375 nm and 425 nm, corresponding to the absorption peak and edge, respectively, were obtained via TMM simulations and are plotted in Figs. 2a, b, e, and f. The electric field distributions within the devices for the wavelength range of 200-700 nm were obtained via 3D-FDTD simulations and are shown in Figs. 2c, d, g, and h.

As shown in Fig. 2a, while the two wavelengths of light interact differently with the Device 150-1:1 active layer, both generate excitons throughout the layer. The strong absorption of light at 375 nm results in a high exciton generation rate of 2.1 x 10^{19} $s^{-1}cm^{-3}$ at the PEDOT:PSS/active layer interface. Despite the quick decay, this light still produces significant exciton generation rates throughout the entire active layer, only dropping below 10^{18} $s^{-1}cm^{-3}$ within the top 10 nm of the active layer. Light at 425 nm induces a smaller exciton generation rate of 1.4 x 10^{19} $s^{-1}cm^{-3}$ at the PEDOT:PSS/active layer interface since it is near the edge of the absorption peak. The weak absorption by the active layer enables the light to penetrate the entire layer and reflect off the Al anode, establishing an interference pattern with a period of 106 nm. This interference leads to bulk exciton generation throughout the entire active layer, with peaks around 1.4 x 10^{19} $s^{-1}cm^{-3}$. Similar behavior is observed in Fig. 2b for Device 200-2:1. Again, light at 375 nm induces a high exciton generation rate of 1.7 x 10^{19} $s^{-1}cm^{-3}$ at the PEDOT:PSS/active layer interface, which decays throughout the active layer but stays above 10^{18} $s^{-1}cm^{-3}$ until the top 20 nm of the active layer. Light at 425 nm does not induce significant exciton generation at the PEDOT:PSS/active layer interface. This is because of the interference pattern, which has the same period of 106 nm due to the similarity between the optical constants for the 1:1 and 2:1 weight ratio blends, as shown in Fig. S2. As in Device 150-1:1, light at 425 nm establishes bulk exciton generation in Device 200-2:1 with peaks throughout the active layer around 6 x 10^{18} $s^{-1}cm^{-3}$. The exciton generation rate in Device 200-2:1 is generally smaller than that in Device 150-1:1, so a weaker photoresponse is expected from Device 200-2:1. Because light of both simulated wavelengths generates excitons throughout the active layers, we expect these two thin devices to exhibit broad photoresponse when exposed to any light within the absorption range. The FDTD-simulated electric fields throughout Devices 150-1:1 and 200-2:1 (Figs. 2 c and d) further support the expectation of a broad UV response for both thin devices. An electric field is present throughout the entirety of both active layers, for the wavelength range of ~250-420 nm, indicating that these devices will respond strongly to any light within this range. The electric field present in Device 200-2:1 (Fig. 2d) is slightly weaker than that in Device 150-1:1 (Fig. 2c), supporting the expectation that Device 150-1:1 will produce a stronger photoresponse than Device 200-2:1.

TMM simulations were performed at the same two wavelengths for Devices 1900-1:1 and 1400-2:1, shown in Figs. 2e and f. For Device 1900-1:1 (Fig. 2e), light at 425 nm still penetrates the entire active layer, establishing an interference pattern with a 105 nm period and bulk exciton generation with peaks that decay throughout the active layer but average around 1.6 x 10^{18} $s^{-1}cm^{-3}$. Because the exciton generation rate is sustained throughout the active layer, a photoresponse is expected from Device 1900-1:1 at this wavelength of 425 nm. The exciton generation rate induced by 375 nm light is still high, with a value of 1.9 x 10^{19} $s^{-1}cm^{-3}$, at the PEDOT:PSS/active layer interface. However, it falls off very quickly, dropping below 10^{18} $s^{-1}cm^{-3}$ within the first 150 nm of the active layer, which is less than 10% of its total width. Similar behavior is

observed from Device 1400-2:1, shown in Fig. 2f. Light at 375 nm again induces a strong exciton generation rate of 1.8 x 10^{19} $s^{-1}cm^{-3}$ at the PEDOT:PSS/active layer interface, but it drops off quickly and falls below 10^{18} $s^{-1}cm^{-3}$ about 150 nm into the active layer, which in this case is just over 10% of its total width. Light at 425 nm establishes a bulk exciton generation rate with the same period of 105 nm and peaks throughout the active layer averaging around 2.7 x 10^{18} $s^{-1}cm^{-3}$. This

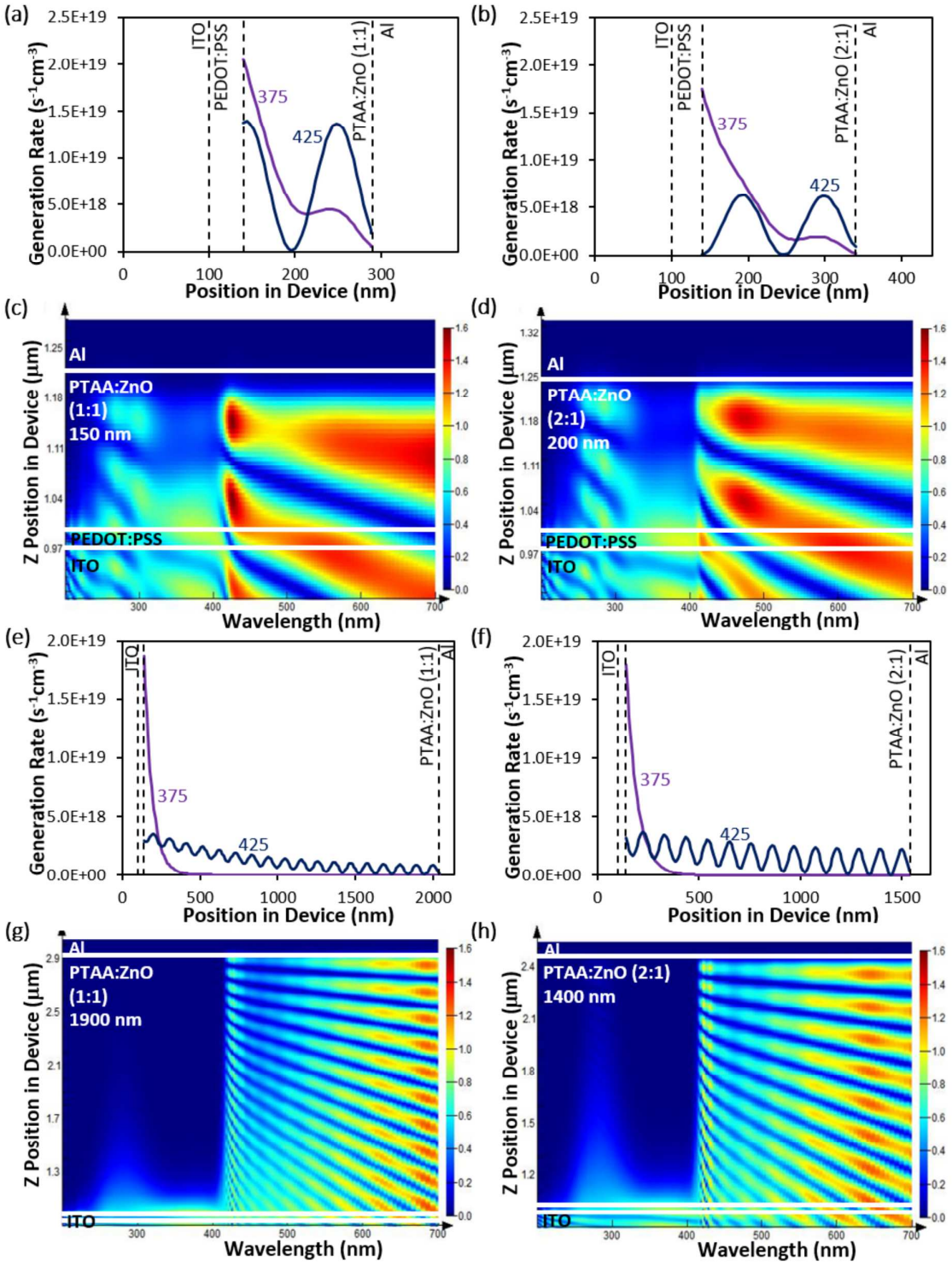

Fig. 2 TMM-simulated exciton generation rate throughout the active layer for (a) Device 150-1:1, (b) Device 200-2:1, (e) Device 1900-1:1, and (f) Device 1400-2:1. 3D-FDTD-simulated electric field distribution throughout the device as a function of incident wavelength for (c) Device 150-1:1, (d) Device 200-2:1, (g) Device 1900-1:1, and (h) Device 1400-2:1.

exciton generation rate is slightly higher than that of Device 1900-1:1, so a slightly stronger photoresponse at 425 nm is expected for Device 1400-2:1, compared to Device 1900-1:1. For both thick devices, under illumination by light within the absorption peak, the strong absorption causes excitons to only be generated within a small portion of the active layer close to the PEDOT:PSS layer. This unbalanced exciton generation creates a space charge and therefore a barrier to charge transfer, so no significant photoresponse should be observed at these wavelengths[10]. Therefore, a narrowband photoresponse centered around 425 nm, which generates excitons throughout the entire active layer, is expected from Devices 1900-1:1 and 1400-2:1. The exciton generation rates produced by both thick devices are smaller than those produced by thin devices, and thus the thin devices should generally produce a stronger photoresponse than thick devices. The expectation for the photoresponse to narrow with increasing thickness is also supported by the FDTD-simulated electric fields, shown in Figs. 2g and h. For Device 1900-1:1 (Fig. 2g), the electric field oscillates at the absorption edge of the active layer, around 425 nm, and is therefore strong throughout the entire active layer. The electric field falls off quickly in the rest of the UV range, with wavelengths below 425 nm, and does not extend significantly into the active layer due to the active layer absorption. Therefore, a photoresponse is only expected at the absorption edge wavelength of 425 nm. The same phenomenon is observed for Device 1400-2:1 (Fig. 2h), but it is not as clean. In fact, the electric field does extend, albeit weakly, throughout the active layer for wavelengths around 270-300 nm, indicating that a photoresponse may be observed for these wavelengths. The electric field overall is stronger for Device 1400-2:1 than it is for Device 1900-1:1, so it is again expected that Device 1400-2:1 will produce a stronger photoresponse than Device 1900-1:1, but the narrowing of the response may not be as clean.

Experimentally, we fabricated devices with thin and thick PTAA:ZnO active layers and measured their EQE spectra under reverse biases, shown in Fig. 3. Generally, as predicted by the simulation results in Fig. 2, thin devices produce a broad UV response with high EQE values compared to the weaker, narrower response of the thick devices. Device 150-1:1 (Fig. 3a) produces the highest EQE values with a peak of 295% under 350 nm illumination and a -1 V bias. Device 200-2:1 (Fig. 3b) shows a lower peak value of 21% under 350 nm illumination and a -1 V bias due to both the composition and the slightly thicker active layer compared to Device 150-1:1. The lower EQE values obtained from Device 200-2:1 compared to those from Device 150-1:1 are consistent with the trend predicted by the TMM and FDTD simulations even though no bias was considered in simulations. With a significantly thicker active layer, Device 1900-1:1 (Fig. 3c) shows good response-narrowing to the edge of the PTAA absorption with a remarkably low FWHM of 12 nm, but a much lower EQE of 0.66% under 424 nm illumination and a -1 V reverse bias. Device 1900-1:1 maintained stable behavior under stronger applied biases and an EQE value of 2.8% was achieved under 424 nm illumination and a -10 V bias. However, the stronger bias increased photoresponse throughout the UV range,

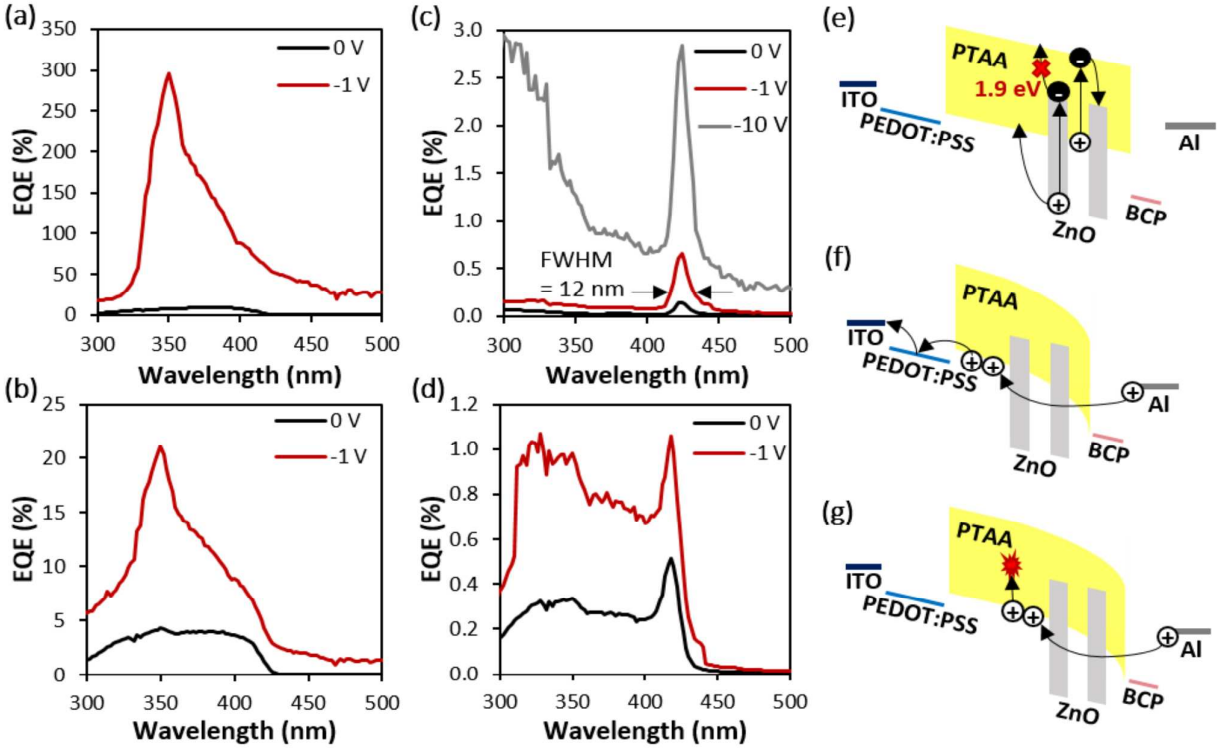

Fig. 3 EQE spectra for (a) Device 150-1:1, (b) Device 200-2:1, (c) Device 1900-1:1, and (d) Device 1400-2:1 under zero and reverse biases. Schematic illustration of (e) exciton generation in PTAA and ZnO and electron trapping in ZnO nanoparticles, (f) band bending and hole injection from the Al cathode, and subsequent collection of holes at the anode in a thin device, and (g) band bending and hole injection from the Al cathode and subsequent hole loss to recombination in a thick device.

specifically producing EQE values above 1% for wavelengths shorter than 350 nm. The FWHM for the EQE peak for this device remains narrow, below 16 nm, under subsequent testing with applied reverse biases up to -16 V, as shown in Fig. S3, and is therefore determined to be a stable feature of the photoresponse. While Device 1400-2:1 (Fig. 3d) produced a narrow EQE peak centered around 418 nm with a value of 1.1% under a -1 V bias, the response throughout the UV range of 310-410 nm was maintained with EQE values between 0.7-1%.

As observed in Fig. 3a, photomultiplication, the collection of multiple charge carriers per incident photon, is achieved in Device 150-1:1. By the definition of EQE, that is the ratio of charge carriers collected per incident photon, the achievement of photomultiplication yields EQE values over 100%. In Device 150-1:1, photomultiplication occurs through charge trapping, band bending, and charge injection – a mechanism that has been well studied and evaluated in organic and inorganic-organic hybrid devices with active layer thicknesses in the range of 200-500 nm. The EQE values produced by Device 150-1:1 in this work, given the low applied bias, are comparable to those produced by similar systems in the literature utilizing the same photomultiplication mechanism. The organic system of P3HT and $PC_{71}BM$, blended with a weight ratio of 100:1, was utilized in devices with a structure of ITO/PEDOT:PSS/P3HT:$PC_{71}BM$/LiF/Al to obtain EQE values of 16,700% under 380 nm illumination and a -19 V bias through this photomultiplication mechanism[22]. This EQE was further increased to over 35,000% under the same conditions by removing the LiF electron transport/hole-blocking layer[23, 24]. The same mechanism was utilized in a more UV-selective system composed of a blend of poly(9,9-dioctylfluorene-alt-bithiophene) (F8T2) and $PC_{71}BM$ with a weight ratio of 100:4 to achieve EQE values of 5600% under 360 nm illumination and a -40 V bias[25]. Organic-inorganic hybrid systems, particularly polymer-nanoparticle blends, have also been employed to take advantage of this photomultiplication mechanism. Blending CdTe nanoparticles into a P3HT:$PC_{61}BM$ film yielded a peak EQE of 8000% under 350 nm illumination and a -4.5 V bias[9]. Additionally, ZnO nanoparticles have been incorporated into both P3HT and PVK active layers in devices with the structure ITO/PEDOT:PSS/PVK:4,4'-bis[(p-trichlorosilylpropylphenyl) phenylamino]-biphenyl (TPD-Si2)/(PVK or P3HT):ZnO/BCP/Al[26]. These devices produced a strong UV photoresponse corresponding to the optical absorption of each active layer. The PVK:ZnO device produced a more UV-specific response, covering a range of ~300-375 nm and peaking around 245,300% under 360 nm illumination and a -9 V bias, while the P3HT:ZnO device produced a broader response from about 325 to 650 nm, peaking around 340,600% under 360 nm illumination and a -9 V bias, due to the narrower bandgap of P3HT compared to PVK[26].

The photomultiplication observed in Device 150-1:1 supports the idea that ZnO nanoparticles are isolated within the PTAA layer, because this is essential to the photomultiplication mechanism as illustrated in Fig. 3e-g. In the active layers, both PTAA and ZnO nanoparticles can absorb light, while PTAA acts as a hole transport material and the ZnO nanoparticles act as electron traps. Fig. 3e shows the exciton generation that occurs in the active layer upon illumination under an applied reverse bias. When the device is illuminated with light at wavelengths between 350 and 420 nm, excitons are generated in PTAA and diffuse throughout the active layer until they either recombine or come to an interface with ZnO. At this point the exciton can dissociate. The hole remains in the PTAA and moves through the active layer towards the ITO anode to be collected. The electron, however, is trapped in the isolated ZnO nanoparticle with a significant barrier of 1.9 eV to escape into the LUMO of PTAA. For illumination with light at wavelengths shorter than 350 nm, excitons can be generated in ZnO, in addition to PTAA. In this case, the electron is still trapped in the isolated ZnO nanoparticle by the same barrier to escape, but the hole can easily transfer into the HOMO of PTAA and move through the active layer to be collected at the anode. The trapped electrons in ZnO bend down the active layer energy bands, shortening the tunneling distance and therefore lowering the barrier for holes to be injected from the Al cathode into the HOMO of PTAA (Figs. 3f and g). In thin devices, illustrated in Fig. 3f, these injected holes can move through the active layer and be collected at the ITO anode. Multiple holes can be injected per incident photon, so this mechanism can lead to photomultiplication and an EQE over 100%. Generally, the thick devices produce much lower EQE values for two reasons: (1) the overall decrease in exciton generation rate compared to thinner devices, shown in Fig. 2, and (2) the increased likelihood of charge recombination accompanying significant increases in film thickness, as illustrated in Fig. 3g.

A few features of the photoresponse spectra of the thick devices in this work should be noted. First, the peak response of the thick devices occurs at a slightly longer wavelength than the absorption edge shown in Fig. 1b. As film thickness increases, a longer wavelength is required for light to penetrate through the active layer, resulting in a redshift in photoresponse[10]. Additionally, compared to the suppression of broad UV response achieved by Device 1900-1:1 under the same -1 V bias, the narrowing is not clean for Device 1400-2:1. This can be explained with the FDTD-simulated electric fields for Devices 1900-1:1 and 1400-2:1 (Figs. 2g and h). Both devices have a significant electric field throughout the active layer at longer wavelengths, starting around the absorption edge, so both devices exhibit photoresponse at the edge of their absorption range. In reality, this occurs at the slightly longer wavelength of 424 nm for the thicker, 1900 nm active layer in Device 1900-1:1, compared to the peak response wavelength of 418 nm for the slightly thinner, 1400 nm active layer in Device 1400-2:1. This is because thicker films generally experience a redshift in their absorption[10]. It is clear in Figs. 2g and h that the electric field throughout the active layer in most of the UV range, with wavelengths shorter than 425 nm, is weaker in Device 1900-1:1 than in Device 1400-2:1, implying a weaker photoresponse throughout this region. From this, it would seem that the weight ratio directly impacts the efficacy of the CCN mechanism, but it is plausible that the difference

between the clean narrowing of Device 1900-1:1 and the broader response of Device 1400-2:1 could solely be due to the difference in film thickness. Experimentally, the effects of thickness and composition could not be easily isolated due to the difficulty in obtaining the same thickness for different compositions via spin speed variation. We therefore used FDTD simulations to evaluate the electric field distributions for devices with both weight ratios of 1:1 and 2:1 at each thickness of 1400 and 1900 nm, shown in Fig. S4. For each weight ratio, increasing the thickness of the active layer from 1400 nm (Figs. S4a and b) to 1900 nm (Figs. S4c and d) caused the electric field to decrease within the absorption peak, indicating that the photoresponse will be weaker at these wavelengths and the CCN mechanism will be more effective. Additionally, for each active layer thickness, the devices with a 1:1 weight ratio (Figs. S4a and c) exhibit a weaker electric field throughout the absorption peak than the devices with a 2:1 weight ratio (Figs. S4b and d), indicating that at any thickness, a device with a 1:1 weight ratio will engage the CCN mechanism more effectively and produce a cleaner response-narrowing than a device with a 2:1 weight ratio. From these comparisons, it can be determined that both the increase in active layer thickness and the 1:1 weight ratio of PTAA:ZnO produce the superior photoresponse-narrowing observed in Device 1900-1:1 compared to Device 1400-2:1.

It also important to note that the photocurrent obtained from the devices in this work, both thick and thin, can be increased by applying a stronger reverse bias, as demonstrated in Fig. 3c and Fig. S3. This is due to an increase in the internal electric field, aiding the movement of holes through the active layer and improving the likelihood that they be collected at the anode. Strong biases have been applied to devices utilizing a blend of P3HT and $PC_{61}BM$ with a weight ratio of 100:1 in active layer thicknesses ranging from 0.3 to 7 μm, combining the response mechanisms of CCN and photomultiplication to produce very narrow, very strong photoresponse[27, 28]. A single, narrow EQE peak exceeding 50,000%, centered around 650 nm with a 30 nm FWHM, was achieved via hole injection from the Al cathode under a -60 V bias[28]. The same devices showed a U-shaped EQE spectrum under a +60 V bias, yielding EQE peaks around 40,000% under 340 nm illumination and 20,000% under 650 nm illumination[27]. Under forward bias, a larger peak was observed near the short edge of the absorption peak because holes were injected from the ITO anode, rather than the Al cathode. Because of this, the photomultiplication mechanism occurred in the portion of the active layer near the anode, so it was engaged by light with a short penetration depth[27].

With stronger applied biases, the EQE values obtained from our devices could be increased to be more competitive with those reported for similar systems, but for the sake of practical applicability, we have focused our evaluation on the low-bias region. For most applications, a small working voltage and minimal energy demands are desirable. Additionally, it has been previously reported[25] and observed in this work that thin devices can become unstable under strong applied biases.

With PTAA:ZnO weight ratios of 1:1 and 2:1, there is a significant amount of ZnO nanoparticles, and the surface states and defects of these nanoparticles need to be considered. The ZnO crystal structure introduces native defects, including vacancies (a missing atom), interstitial sites (an atom outside of a lattice site), and anti-sites (one atom in another's site)[29]. Some of these defects – O vacancies, Zn interstitials, and Zn anti-sites – are donor-like defects that contribute to the inherent n-type behavior of ZnO[29]. These defects, particularly O vacancies at the nanoparticle surfaces, introduce extra electrons into the conduction band that enable the surface to adsorb O_2 from air[30]. Engaging electrons in this adsorption creates a depletion region of lowered conductivity on the ZnO surface, which is particularly impactful for nanoparticles[31, 32]. Under UV illumination and forward bias, the O_2 can be desorbed, freeing the electrons and increasing the conductivity of the ZnO[30]. This can be an effective photoresponse mechanism[32], but only if the dark/neutral-bias behavior can be immediately recovered. Depending on the system and the testing conditions, the conductivity increase is sometimes maintained even when the illumination/forward bias is removed. This is called persistent photoconductivity, and it results in the loss of a distinguishable photoresponse. Stable behavior can often be recovered upon aging in air and/or exposure to strong reverse biases[31].

In this work, when persistent photoconductivity was observed, that is when dark current and photocurrent became indistinguishable, the devices were aged in air until the dark current returned to its original levels. This aging time was typically about 1 day, and then testing continued. Multiple electrodes on each chip were tested to ensure stable, reproducible behavior. Additionally, the dark current was repeatedly checked throughout testing to ensure that the device was stable and that any observed photoresponse was distinct from persistent photoconductivity. The extent to which persistent photoconductivity affected device stability was impacted by the weight ratio of the active layer, as shown in Fig. S5. A pure PTAA device (Fig. S5a) does not experience any persistent photoconductivity, and has stable, reproducible dark current behavior before and after EQE measurements. For devices with a higher ZnO content, persistent photoconductivity was evident and stable behavior could not always be recovered. As shown in Figs. S5b and c, both pure ZnO devices and PTAA:ZnO devices with a weight ratio of 1:10, respectively, exhibited an increase in dark current, especially under reverse biases, after EQE measurements. The increased dark current could not be lowered to the level of freshly made devices even after aging in air or under forward bias. Generally, a higher ZnO content produces higher currents for both dark and illuminated conditions, while a higher PTAA content improves device stability. Considering both factors, the weight ratio of 1:1 was found as optimal among those investigated in this work.

The dark and illuminated current density-voltage characteristics for all four devices are shown in Fig. 4. Generally, as predicted by the simulations in Fig. 2 and observed in the EQE spectra in Fig. 3, the thinner devices (Fig.

4a) produce higher currents under both dark and illuminated conditions than the thick devices (Fig. 4b). For both thin devices, the photocurrent and dark current, shown in Fig. 4a, are only distinguishable within a small bias range, from about -1.5 to 0.7 V, indicating that the device response is not stable outside of this range. Additionally, Device 150-1:1 produces a higher photocurrent than Device 200-2:1, with values of 7.9 x 10^{-4} mA cm^{-2} and 2.4 x 10^{-4} mA cm^{-2} under a -1 V bias and 375 nm illumination, respectively. Both thick devices produce a clearly distinguishable photoresponse throughout the relevant voltage range, with the photocurrent approximately two orders of magnitude greater than the dark current, as shown in Fig. 4b. For Device 1900-1:1, the dark current shows rectification and is very close to the photocurrent under forward bias. Device 1400-2:1 produces a stronger photocurrent than Device 1900-1:1, with values of 5.4 x 10^{-5} mA cm^{-2} and 2.1 x 10^{-5} mA cm^{-2} under a -1 V bias and 420 nm and 424 nm illumination, respectively.

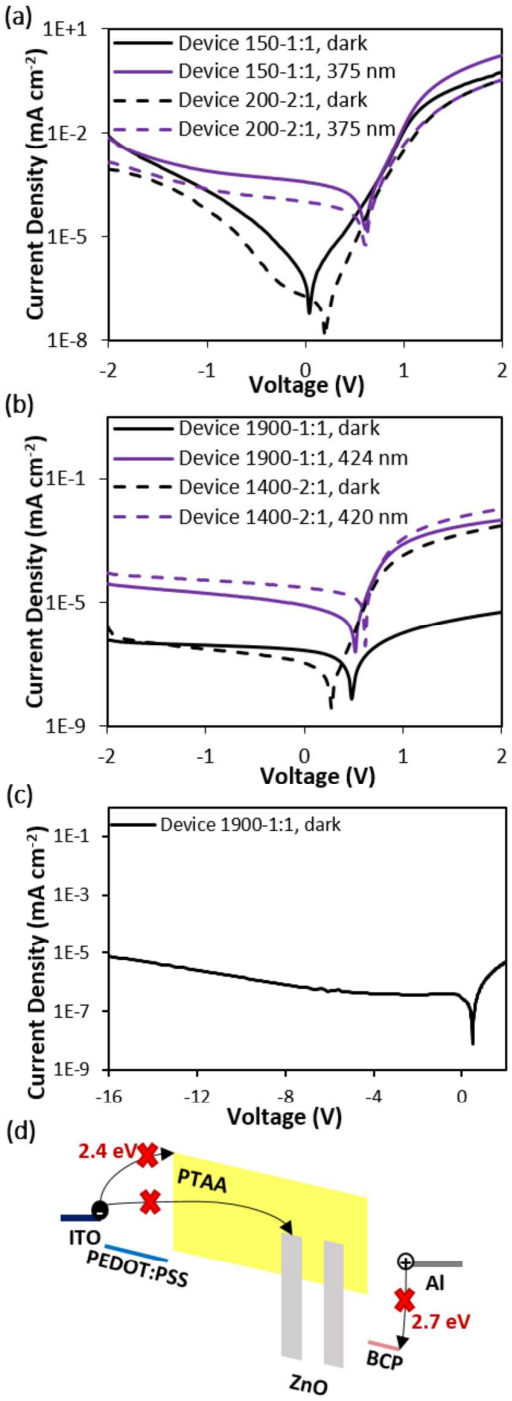

Fig. 4 Dark and illuminated current density-voltage characteristics for (a) Devices 150-1:1 and 200-2:1, and (b) Devices 1900-1:1 and 1400-2:1. (c) Dark current density under strong reverse bias for Device 1900-1:1. (d) Schematic illustration of the barriers to charge injection enabling the low dark current of Device 1900-1:1 to be maintained under strong reverse biases.

For Device 1900-1:1, low dark current below 1 x 10^{-5} mA cm^{-2} can be maintained even at strong reverse biases, shown in Fig. 4c. As illustrated in Fig. 4d, the low dark current is due to the relatively large barrier (2.7 eV) to hole injection from the Al cathode into the BCP layer and the even larger barrier (2.4 eV) to electron injection from the ITO anode into LUMO of PTAA. There could be electron injection from the ITO anode into the conduction band of ZnO based on their energy level alignment (0.5 eV barrier), but this injection is limited because ZnO nanoparticles may not directly contact the PEDOT:PSS interface. Additionally, even if some electrons were injected, they could not be transported through the active layer because the ZnO nanoparticles do not form a continuous pathway.

The dark current of devices is indicative of the noise level that is present, which is obtained from a Fast Fourier Transform (FFT) of the dark current values[33]. Plots of the noise current versus frequency are given in Fig. S6 for each device. For the thin devices, the application of a -1 V bias causes a significant increase in both dark and noise currents. For Device 150-1:1, the dark current increases from 5.0 x 0^{-8} mA cm^{-2} under no bias, to 5.1 x 10^{-3} mA cm^{-2} under a -1 V bias, and the noise current increases from 2.0 x 10^{-13} A $Hz^{-1/2}$ under no bias to 1.3 x 10^{-10} A $Hz^{-1/2}$ under a -1 V bias. Similarly, for Device 200-2:1, the dark current increases from 3.4 x 10^{-7} mA cm^{-2} under no bias to 1.1 x 10^{-5} mA cm^{-2} under a -1 V bias, and the noise current increases from 2.4 x 10^{-13} A $Hz^{-1/2}$ under no bias to 2.0 x 10^{-12} A $Hz^{-1/2}$ under a -1 V bias. For the thicker devices, the impact of bias on the dark and noise currents is much less severe. For Device 1900-1:1, the dark current increases from 4.0 x 10^{-7} mA cm^{-2} under no bias to 6.7 x 10^{-7} mA cm^{-2} under a -1 V bias, and the noise increases mildly from 1.2 x 10^{-13} A $Hz^{-1/2}$ without any bias to 2.7 x 10^{-13} A $Hz^{-1/2}$ under a -1 V bias. Similarly, for Device 1400-2:1 the dark current is increased from 1.9 x 10^{-7} mA cm^{-2} under no bias to 8.9 x 10^{-7} mA cm^{-2} under a -1 V bias, and the noise decreased from 2.4 x 10^{-12} A $Hz^{-1/2}$ under no bias to 5.0 x 10^{-13} A $Hz^{-1/2}$ under a -1 V bias.

The responsivity (R) and specific detectivity (D*) were also calculated for these devices, using equations (1) and (2) below:

$$R = EQE * \frac{q\lambda}{hc}, \quad (1)$$

$$D* = \frac{R\sqrt{A}}{I_n} \quad (2)$$

where q is the elementary charge, λ is the wavelength of incident light, h is Planck's constant, c is the speed of light in vacuum, A is the device active area, and I_n is the noise current. The R and D* results are plotted in Fig. 5, with results for thick and thin devices of the same weight ratios plotted together. As shown in Fig. 5a, Device 150-1:1 obtained a peak R value of 83.2 A W^{-1} under 350 nm illumination and a -1 V bias, while Device 1900-1:1 maintained its narrowband spectral shape, with a peak R value of 0.23 A W^{-1} under 424 nm illumination and a -1 V bias. As shown in Fig. 5b, Device 200-2:1 produced a spectral shape similar to that produced by Device 150-1:1, but much weaker in magnitude, with a peak R value of 5.93 A W^{-1} under 350 nm illumination and a -1 V bias. Device 1400-2:1, also shown in Fig. 5b, again demonstrates CCN, as evidenced by the peak of 0.36 A W^{-1} obtained under 420 nm illumination and a -1 V bias. However, R values around 0.25 A W^{-1} are maintained throughout most of the UV range between about 310-410 nm, indicating that this device does not engage the CCN mechanism as effectively as Device 1900-1:1, due to both its composition and thickness as previously discussed. Because both noise current and photoresponse are accounted for in D*, the values for the thin devices decreased under reverse bias while the values for the thick devices increased. This is because thick devices produced only a slight increase in noise current when a reverse bias was applied, compared to the severe increase in noise current observed when a reverse bias was applied to the thinner devices. As shown in Fig. 5c, for Device 150-1:1 the peak D* value of 3.7 x 10^{12} Jones is obtained without any applied bias, under 382 nm illumination. Also shown in Fig. 5c are D* spectra for Device 1900-1:1. For this device, the applied bias improves D*, which peaks at 2.6 x 10^{11} Jones under 424 nm illumination and a -1 V bias. Similarly, in Fig. 5d it can be seen that Device 200-2:1 also produces its peak D* value of 1.6 x 10^{12} Jones without any applied bias, under 350 nm illumination, whereas for Device 1400-2:1 the peak D* value of 2.3 x 10^{11} Jones is obtained under 420 nm illumination and a -1 V bias.

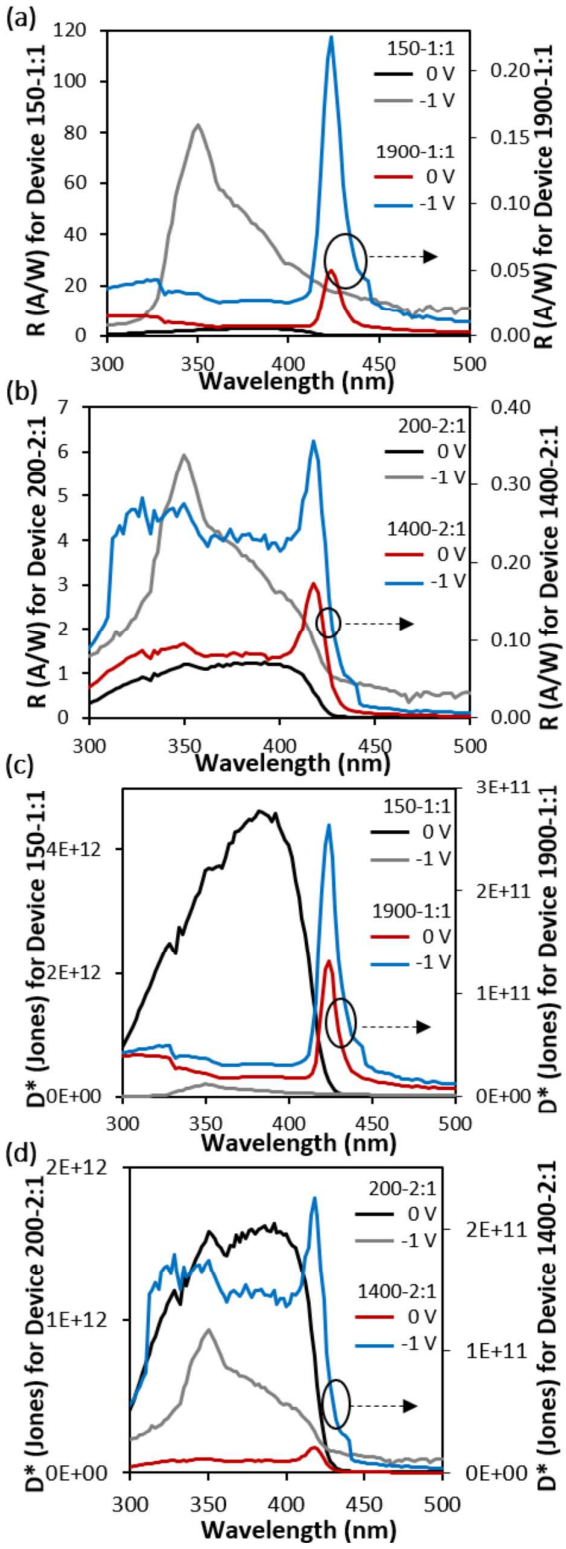

Fig. 5 Responsivity (a and b) and specific detectivity (c and d) under 0 and -1 V biases. Responsivity for (a) Devices 150-1:1 and 1900-1:1, and (b) Devices 200-2:1 and 1400-2:1. Specific detectivity for (c) Devices 150-1:1 and 1900-1:1, and (d) Devices 200-2:1 and 1400-2:1.

The on-off response speed is another important figure of merit for photodetectors and is shown for these devices in Fig. 6. The response was measured under 375 nm illumination for the two thin devices (Device 150-1:1 and Device 200-2:1), and under 424 and 420 nm illumination for Device 1900-1:1 and Device 1400-2:1, respectively. Because Device 150-1:1 produced higher photocurrents than the other devices, its on-off response could be measured with no applied bias. For

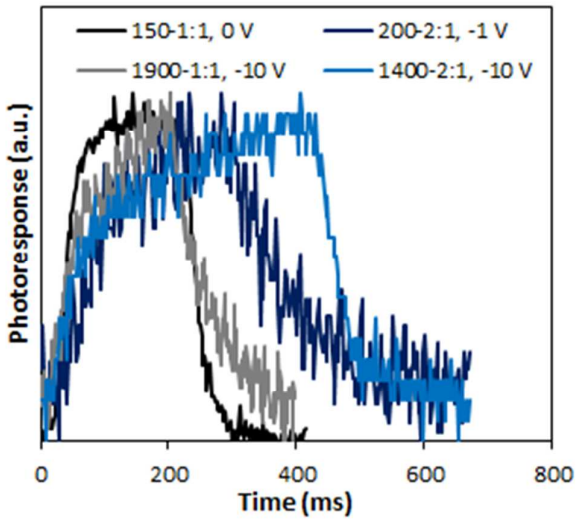

Fig. 6 Photoresponse for (a) Device 150-1:1 under 375 nm illumination, (b) Device 200-2:1 under 375 nm illumination, (c) Device 1900-1:1 under 424 nm illumination, (d) Device 1400-2:1 under 420 nm illumination.

Device 200-2:1, a -1 V bias was applied to produce a sufficient photoresponse for these measurements, and a -10 V bias had to be used for Devices 1900-1:1 and 1400-2:1. Generally, applying a bias should increase the response speed of a device[34]. Therefore, because Device 150-1:1 exhibits the fastest photoresponse when it is tested without any bias and compared to devices under bias, as in Fig. 6, it must have the fastest photoresponse of the devices tested. The rise and fall times for Device 150-1:1 were found to be around 50 and 60 ms, respectively. These response times are slower than the rise and fall times of 25 and 558 μs reported for a P3HT:ZnO system under a -9 V bias[26], but faster than the rise and fall times, below 200 ms, reported for a device based on ZnO nanoparticles embedded in a layer of poly(9,9-dihexylfluorene) (PFH) under a -1 V bias[31].

Conclusions

The effects of active layer film thickness and composition on the spectral response of UV photodetectors have been investigated. TMM and FDTD simulations were used to provide insights into the exciton generation rate and electric field distribution within the devices as a function of incident light wavelength. Experimentally, the active layer film thickness and composition were used to tune between broad and narrow spectral response for UV-selective photodetectors whose active layers are a blend of PTAA and ZnO nanoparticles with the weight ratios of 1:1 and 2:1. Devices with thin active layers (150-200 nm) exhibited a broad photoresponse, while devices with thick active layers (1400-1900 nm) showed a narrowed photoresponse centered at the edge of the absorption peak of the active layer, due to charge collection narrowing. The device with a 1900 nm active layer and PTAA:ZnO weight ratio of 1:1 showed an extremely narrow, single photoresponse peak centered at 424 nm with a FWHM of 12 nm. The corresponding responsivity and specific detectivity were 0.23 A W^{-1} and 2.6 x 10^{11} Jones under 424 nm illumination and a -1 V bias. Decreasing the active layer thickness to 150 nm with the same weight ratio resulted in a broad photoresponse in the wavelength range of ~320-420 nm, with a peak EQE of 295% under 350 nm illumination and a -1 V bias due to the charge trapping and injection enabled by the ZnO nanoparticles acting as electron traps. The photomultiplication produced a peak responsivity of 83.2 A W^{-1} under 350 nm illumination and a -1 V bias, but the peak specific detectivity of 3.7 x 10^{12} Jones was achieved under no bias, and decreased to 2.0 x 10^{11} under a -1 V bias due to the increase of dark and noise currents. Generally, increasing the weight ratio of PTAA:ZnO to 2:1 lowered dark and photocurrent values, eliminated photomultiplication in the thin device, and increased the photoresponse throughout the UV range (between ~310-410 nm) in addition to the narrow peak at the PTAA absorption edge of about 420 nm in the thick device. The CCN mechanism has been effectively extended into the range of UV photodetectors, and the response in this range can be easily tuned between a broad photomultiplicative response and a sensitive and selective narrowband response, simply by varying the thickness and composition of the active layer.

Conflicts of interest

There are no conflicts to declare.

Acknowledgements

This work was supported by the Defense Threat Reduction Agency (HDTRA1-15-1-0021). Part of this work was conducted at the Molecular Analysis Facility, a National Nanotechnology Coordinated Infrastructure (NNCI) site at the University of Washington, which is supported in part by funds from the NSF (EECS-1542101). MRE acknowledges a fellowship from the UW Clean Energy Institute. Some device fabrication steps were carried out in the UW Department of Chemistry's Photonics Research Center. UV–vis absorption and profilometry measurements were conducted in the lab of Professor Samson Jenekhe. photoluminescence measurements were carried out in the UW Department of Chemistry's Spectroscopic and Analytical Instrumentation facility.

References

1. K. J. Baeg, M. Binda, D. Natali, M. Caironi and Y. Y. Noh, *Advanced Materials*, 2013, **25**, 4267-4295.
2. X. Gong, M. H. Tong, Y. J. Xia, W. Z. Cai, J. S. Moon, Y. Cao, G. Yu, C. L. Shieh, B. Nilsson and A. J. Heeger, *Science*, 2009, **325**, 1665-1667.
3. G. Konstantatos and E. H. Sargent, *Nature Nanotechnology*, 2010, **5**, 391-400.
4. N. C. Greenham, X. G. Peng and A. P. Alivisatos, *Physical Review B*, 1996, **54**, 17628-17637.
5. T. Rauch, M. Boberl, S. F. Tedde, J. Furst, M. V. Kovalenko, G. N. Hesser, U. Lemmer, W. Heiss and O. Hayden, *Nature Photonics*, 2009, **3**, 332-336.
6. W. H. Li, H. Guo, Z. Wang and G. F. Dong, *Journal of Physical Chemistry C*, 2017, **121**, 15333-15338.
7. M. Azadinia, M. R. Fathollahi, M. Mosadegh, F. A. Boroumand and E. Mohajerani, *Journal of Applied Physics*, 2017, **122**, 10.
8. L. Shen, Y. J. Fang, H. T. Wei, Y. B. Yuan and J. S. Huang, *Advanced Materials*, 2016, **28**, 2043-+.
9. H. Y. Chen, M. K. F. Lo, G. W. Yang, H. G. Monbouquette and Y. Yang, *Nature Nanotechnology*, 2008, **3**, 543-547.
10. A. Armin, R. D. Jansen-van Vuuren, N. Kopidakis, P. L. Burn and P. Meredith, *Nature Communications*, 2015, **6**, 8.
11. C. Pacholski, A. Kornowski and H. Weller, *Angewandte Chemie-International Edition*, 2002, **41**, 1188-+.
12. G. F. Burkhard, E. T. Hoke and M. D. McGehee, *Advanced Materials*, 2010, **22**, 3293-+.
13. G. F. Burkhard and E. T. Hoke, *Transfer Matrix Optical Modeling*, McGehee Group, Stanford Univ., 2011.
14. I. D. Parker, *Journal of Applied Physics*, 1994, **75**, 1656-1666.
15. M. Skompska, *Synthetic Metals*, 2010, **160**, 1-15.
16. H. B. Michaelson, *Journal of Applied Physics*, 1977, **48**, 4729-4733.

17. B. R. Saunders and M. L. Turner, *Advances in Colloid and Interface Science*, 2008, **138**, 1-23.
18. Y. Xu and M. A. A. Schoonen, *American Mineralogist*, 2000, **85**, 543-556.
19. A. B. Djurisic, A. M. C. Ng and X. Y. Chen, *Progress in Quantum Electronics*, 2010, **34**, 191-259.
20. S. N. Habisreutinger, T. Leijtens, G. E. Eperon, S. D. Stranks, R. J. Nicholas and H. J. Snaith, *Nano Letters*, 2014, **14**, 5561-5568.
21. I. McCulloch and M. Heeney, Material Matters2009, vol. 4.3.
22. L. L. Li, F. J. Zhang, J. Wang, Q. S. An, Q. Q. Sun, W. B. Wang, J. Zhang and F. Teng, *Scientific Reports*, 2015, **5**, 7.
23. L. L. Li, F. J. Zhang, W. B. Wang, Y. J. Fang and J. S. Huang, *Physical Chemistry Chemical Physics*, 2015, **17**, 30712-30720.
24. L. L. Li, F. J. Zhang, W. B. Wang, Q. S. An, J. Wang, Q. Q. Sun and M. Zhang, *Acs Applied Materials & Interfaces*, 2015, **7**, 5890-5897.
25. M. R. Esopi, M. Calcagno and Q. M. Yu, *Advanced Materials Technologies*, 2017, **2**, 9.
26. F. W. Guo, B. Yang, Y. B. Yuan, Z. G. Xiao, Q. F. Dong, Y. Bi and J. S. Huang, *Nature Nanotechnology*, 2012, **7**, 798-802.
27. J. L. Miao, F. J. Zhang, M. D. Du, W. B. Wang and Y. Fang, *Physical Chemistry Chemical Physics*, 2017, **19**, 14424-14430.
28. W. B. Wang, F. J. Zhang, M. D. Du, L. L. Li, M. Zhang, K. Wang, Y. S. Wang, B. Hu, Y. Fang and J. S. Huang, *Nano Letters*, 2017, **17**, 1995-2002.
29. F. Oba, M. Choi, A. Togo and I. Tanaka, *Science and Technology of Advanced Materials*, 2011, **12**, 14.
30. X. G. Zheng, Q. S. Li, W. Hu, D. Chen, N. Zhang, M. J. Shi, J. J. Wang and L. C. Zhang, *Journal of Luminescence*, 2007, **122**, 198-201.
31. H. G. Li, G. Wu, M. M. Shi, L. G. Yang, H. Z. Chen and M. Wang, *Applied Physics Letters*, 2008, **93**, 3.
32. Y. Z. Jin, J. P. Wang, B. Q. Sun, J. C. Blakesley and N. C. Greenham, *Nano Letters*, 2008, **8**, 1649-1653.
33. X. B. Xu, C. C. Chueh, P. F. Jing, Z. B. Yang, X. L. Shi, T. Zhao, L. Y. Lin and A. K. Y. Jen, *Advanced Functional Materials*, 2017, **27**, 6.
34. S. O. Kasap, *Principles of Electronic Materials and Devices*, McGraw-Hill, New York, NY, 2006.